

(H,Li)₆Ru₂O₆ : a zero-field Ru³⁺-based Kitaev Quantum Spin Liquid

Sanjay Bachhar,^{1,*} M. Baenitz,² Hubertus Luetkens,³ Sumiran Pujari,¹ and A.V. Mahajan^{1,†}

¹Department of Physics, Indian Institute of Technology Bombay, Powai, Mumbai 400076, India

²Max Planck Institute for Chemical Physics of Solids, 01187 Dresden, Germany

³Laboratory for Muon Spin Spectroscopy, Paul Scherrer Institute, CH-5232 Villigen PSI, Switzerland

We report the synthesis and properties of (H,Li)₆Ru₂O₆, which is shown to be a $J_{\text{eff}} = \frac{1}{2}$ system made out of Ru³⁺ moments in a honeycomb geometry. Bulk magnetization, heat capacity, nuclear magnetic resonance (NMR), and muon spin relaxation (μ SR) rule out the presence of static moments or any spin glass phase down to 500 mK. All techniques suggest a crossover to a liquid-like state below about 40 K. The ⁷Li nuclear magnetic resonance (NMR) shift data suggest a non-zero T -independent spin susceptibility at low T . In zero field, C_m/T shows T^{-1} divergence which is consistent with vacancy-induced effects on low-energy excitations of the pristine Kitaev spin liquid. With field, power-law variations in the ⁷Li NMR spin-lattice relaxation rate $1/T_1$ and magnetic heat capacity C_m show quantitatively new scaling behaviors. A two-step entropy release in heat capacity is also observed putatively from Z_2 flux (low- T step) and itinerant Majorana fermions (high- T step). Based on these findings, we propose that (H,Li)₆Ru₂O₆ realizes a Kitaev spin liquid with no evidence of inherent magnetic ordering in zero field unlike α -RuCl₃ where a ~ 8 Tesla field is required to suppress magnetic order.

Introduction.— Kitaev quantum spin liquids (KQSL) continue to evoke interest due to their novel and exotic ground state and excited state properties [1–5]. They are expected to harbor itinerant Majorana fermion excitations which, apart from being intrinsically interesting, are thought to be useful for quantum computing. An example of a promising Kitaev material is the layered, honeycomb material α -RuCl₃ [6–8] which however undergoes magnetic ordering around 7 K and requires fields greater than about 80 kOe [6] to reveal KQSL features. It has been a challenge to find a material with KQSL physics in absence of magnetic field in general including Ru-based compounds. α -Li₂IrO₃ is another promising KQSL candidate material which again shows AFM ordering below $T_N \sim 15$ K [9]. Takagi *et al.* [10] showed that hydrogen intercalation in α -Li₂IrO₃ results in the formation of H₃LiIr₂O₆ which shows KQSL behaviour with novel low-energy excitations. Given the requirement of a large spin-orbit coupling for Kitaev materials, $4d/5d$ -based honeycomb lattice systems are good starting points to look for new Kitaev systems, for instance moments from Ir⁴⁺/Ru³⁺ with d^5 configuration and $J_{\text{eff}} = \frac{1}{2}$ moments [2, 11–14]. In the iridate case, longer intercalation times starting from α -Li₂IrO₃ gives H₅LiIr₂O₆ [15] which however contains Ir³⁺ ($5d^4$, $J_{\text{eff}} = 0$). There are relatively fewer compounds with Ru³⁺ [14, 16] with α -RuCl₃ being the only honeycomb example. With this background, we set out to prepare H₅LiRu₂O₆ ((H,Li)₆Ru₂O₆) by intercalating excess H in Li₂RuO₃ as a possible Kitaev material. We obtained (H,Li)₆Ru₂O₆ with a honeycomb network of Ru³⁺ as in α -RuCl₃. However, unlike α -RuCl₃, (H,Li)₆Ru₂O₆ intriguingly shows no sign of magnetic order down to about 500 mK. Our measurements pertaining to the magnetism of this new compound find the emergence of a KQSL state at temperatures below 40 K with gapless

excitations.

Before going into the details of the measurements, we discuss some relevant details about the structure of the compound. Previously, silver intercalation in Li₂RuO₃ led to Ag₃LiRu₂O₆ with Ru⁴⁺ [17]. That compound crystallizes in $C2/m$ space group and there was no sign of dimerization unlike Li₂RuO₃ [17–19]. Ag₃LiRu₂O₆ is possibly an example of honeycomb quantum magnet of Khaliullin type (excitonic magnetism in $4d^4$ based system)[17, 19–22]. Instead of the heavier Ag, a lighter and smaller H can be intercalated in excess amount as observed in H₅LiIr₂O₆. Excess H-intercalation in Li₂RuO₃ leads to the replacement of all the inter-layer Li atoms by H atoms and also of a fraction of the in-plane Li atoms. There is a contraction of the c -parameter of the lattice (from 5.13 Å to 5.01 Å) due to the lighter and smaller H atoms replacing the inter-layer Li atoms (see the supplementary materials (SM) [23]). The c -axis shortening does tune the magnetism as observed in H₃LiIr₂O₆, a KQSL (c -parameter reduced from 5.12 Å to 4.87 Å after H-intercalation in Li₂IrO₃). The structural analysis of HLRO reveals a nearly perfect honeycomb network with a Ru-Ru bond distance of ~ 2.96 Å and a $d-p-d$ bond angle of $\sim 95^\circ$. The presence of Ru³⁺ ($J_{\text{eff}} = 1/2$) is inferred from x-ray photoelectron spectroscopy (XPS) analysis. See Fig. 1 (see SM [23] for further details). Also, an entropy recovery of $R \ln 2$ (by about 100 K) is seen in our specific heat data consistent with $J_{\text{eff}} = \frac{1}{2}$ magnetic moments. Li-quantification through ⁷Li NMR Spectral analysis (see SM [23]) in (H,Li)₆Ru₂O₆ led us to the chemical formula, H_{5.9}Li_{0.1}Ru₂O₆ [23] to be referred to as HLRO in the rest of the paper.

Our main findings on the magnetism of HLRO are as follows: Bulk magnetization, heat capacity, NMR, μ SR rule out the presence of static moments or any spin glass

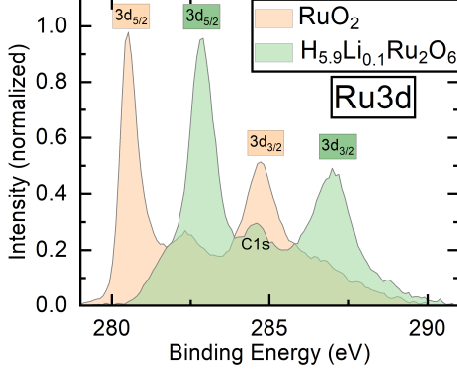


FIG. 1. Ru3d XPS Spectra of $H_{5.9}Li_{0.1}Ru_2O_6$ where binding energies of $3d_{5/2}$ (282.9 eV) and $3d_{3/2}$ (287 eV) are similar to α - $RuCl_3$ (Ru is in +3 oxidation state)[24]. Also, Ru3d XPS spectra of RuO_2 (Ru is in +4 oxidation state) is shown for comparison and binding energies are consistent with literature [24]. C(1s) reference position was taken 284.7 eV for both materials.

phase down to 500 mK. There is a crossover to a liquid-like state below about 40 K. The zero-field divergence of the magnetic heat capacity divided by temperature ($\frac{C_m}{T}$) is consistent with a KQSL scenario in presence of vacancies. $\frac{C_m}{T}$ also shows scaling with increasing field which has been phenomenologically modeled. 7Li NMR shift is non-zero and T -independent indicating a Pauli-like spin susceptibility at low- T as seen in many QSLs. NMR spin-lattice relaxation rates show a power-law variation consistent with gapless excitations. Finally, a two-step magnetic entropy release is observed suggestive of Z_2 flux excitations at low- T and itinerant Majorana fermions at high- T .

Results and discussion.— The bulk magnetic susceptibility of HLRO is shown in Fig. 2. It shows a Curie-Weiss like increase with decreasing temperature and a crossover around 40 K below which the susceptibility continues to increase. No sharp anomaly suggestive of absence of long-range order is observed down to 2 K. A Curie-Weiss fit ($\chi = \chi_0 + \frac{C}{T - \theta_{CW}}$) in the temperature range 100-300 K gives $\chi_0 = 3.69 \times 10^{-5} \text{ cm}^3/\text{mol-Ru}$, $\theta_{CW} \sim -44 \text{ K}$ and effective moment $\mu_{eff} \sim 0.43 \mu_B$. Absence of a bifurcation in the magnetic susceptibility between zero field cooled (ZFC) and field cooled (FC) mode in a small applied field of $H = 50 \text{ Oe}$ in the temperature range 100 K to 2 K rules out the possibility of static/glassy moments present in the system (see SM [23]).

Next, we present results of NMR which is a powerful local probe of intrinsic spin susceptibility and low-energy excitations. The 7Li NMR shift (7K) as function of temperature is shown in Fig. 3 inset. There is a crossover around $T \sim 40 \text{ K}$ similar to that in bulk

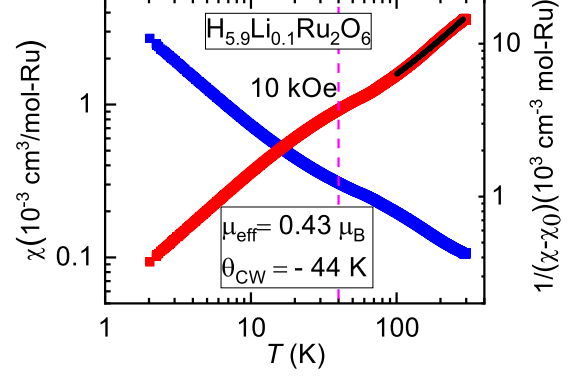


FIG. 2. (a) The left y -axis shows the temperature dependence of the susceptibility, $\chi(T) \equiv \frac{M(T)}{H}$ (blue squares) of $H_{5.9}Li_{0.1}Ru_2O_6$ measured in a field of 10 kOe in zero field cooled (ZFC) condition and the right y -axis shows the inverse susceptibility, χ_0 . The black solid line on red square symbols of $1/(\chi - \chi_0)$ shows the Curie-Weiss fit in the temperature range 100-300 K.

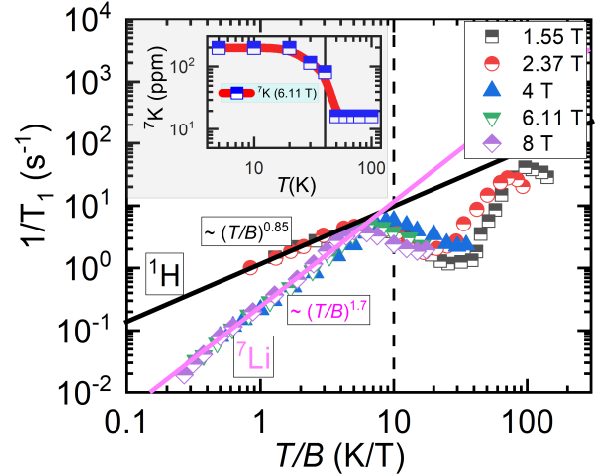


FIG. 3. The temperature-field scaling of the 7Li NMR spin-lattice relaxation rate, $1/{}^7T_1$, with exponent ~ 1.7 and 1H NMR spin-lattice relaxation rate, $1/{}^1T_1$, with exponent ~ 0.85 for $H_{5.9}Li_{0.1}Ru_2O_6$. The data for 1H are multiplied by 13.24 for better presentation. (Inset) 7Li -NMR Shift, 7K with T with crossover around 40 K (solid vertical line).

susceptibility (Fig. 2) and then it levels off down to the lowest temperature. Such T -independent variation has been seen in many QSLs. We have also measured 1H -NMR. No NMR-shift was observed for 1H down to the lowest temperature similar to $H_3LiIr_2O_6$ possibly due to weak hyper-fine coupling. The variation of 1H and 7Li NMR $1/T_1$ as a function of temperature for HLRO in various applied magnetic fields is shown in Fig. 3. A crossover is again seen at $\sim 40 \text{ K}$ similar to other

measurements. Below 40 K, $1/T_1$ exhibits a power law variation with temperature. While the crossover at ~ 40 K is not due to long-range ordering or glassy magnetism, the power-law variation below 40K indicates gapless excitations. Furthermore, $1/T_1$ scales with T/B with an exponent ~ 1.7 for ^7Li and 0.85 for ^1H (Fig. 3) that can be phenomenologically attributed to field-dependent density of states [10].

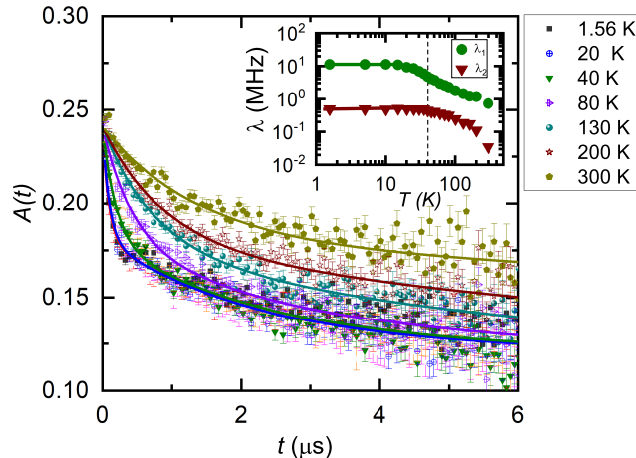


FIG. 4. Muon asymmetry as a function of time in a 100 Oe longitudinal field in the temperature range: 1.56 K-300 K. (Inset) Muon relaxation rate λ as a function of temperature. Two components of relaxation, λ_1 (olive circles) and λ_2 (wine triangles) with $A_1/A_2 \sim 1$ are observed.

Another piece of evidence we now present is that of local moment dynamics in HLRO through μSR measurements which were carried out at the GPS facility in PSI, Switzerland. Zero field (ZF) muon depolarisation data [23] show an exponential decay with no hint of oscillations down to 1.56 K. This indicates the absence of long range ordering consistent with our other measurements. The absence of $1/3$ -tail in muon asymmetry signals that the moments remain dynamic throughout. Since ZF measurements include a contribution from nuclear moments, we have also taken data in a longitudinal field (LF) of 100 Oe to remove the depolarisation due to nuclear moments. This is shown in Fig. 4. We could fit this purely electronic contribution to the muon relaxation asymmetry well using $A(t) = A_1 e^{-\lambda_1 t} + A_2 e^{-\lambda_2 t} + A_3$ [23]. The two components of relaxation (λ_1 and λ_2) occur with nearly equal relative weights ($A_1/A_2 \sim 1$) independent of temperature as shown in the inset of Fig. 4. This is likely due to the presence of two muon stopping sites [25]. The muon relaxation rate increases gradually with decreasing temperature and finally levels off below about 40 K indicating that the spins remains dynamic down to low-

T . These results are similar to those of $\text{H}_3\text{LiIr}_2\text{O}_6$ [26]. Note that the flattening of λ in HLRO sets in at 10 times the temperature in $\text{H}_3\text{LiIr}_2\text{O}_6$ allowing for a larger temperature range to probe KQSL dynamics.

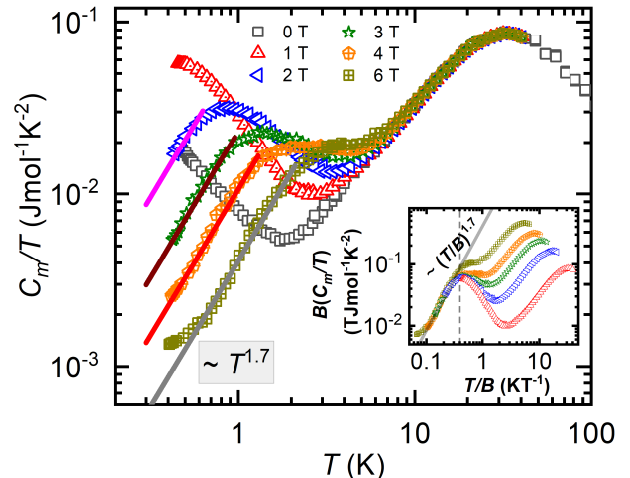


FIG. 5. Magnetic specific heat, C_m/T versus T for various fields B (0-6 Tesla). (Inset) A scaling plot: $B(C_m/T)$ versus T/B with exponent ~ 1.7 for $\text{H}_{5.9}\text{Li}_{0.1}\text{Ru}_2\text{O}_6$.

Finally, we discuss the heat capacity $C_p(T)$ of HLRO. The magnetic piece (C_m) is obtained by subtracting the C_p of a non-magnetic analog [23]. In zero magnetic field, no sharp anomaly is seen in C_m down to 500 mK in agreement with our earlier conclusion of no long-range magnetic order. Furthermore, a non-zero C_m was seen down to the lowest temperature measured indicating the absence of a spin gap. Fig. 5 shows C_m/T as a function of T . In zero magnetic field, $C_m/T \propto T^{-1}$ below about 2 K. A rationale for such a variation has been theoretically proposed in Ref. [3] to arise from small amounts of vacancies and quasi-vacancies in a KQSL. The picture is that the ground state has bound Z_2 -flux in low fields in the presence of vacancies. The zero-flux KQSL is obtained upon the application of magnetic field. With the application of a magnetic field above 1 T, C_m/T follows a power-law scaling as $(T/B)^\gamma$ as shown in the inset of Fig. 5 with $\gamma \sim 1.7$. This is consistent with gapless excitations which we ascribe to the the zero-flux KQSL and weak localization of Majorana fermions [3, 5].

We can account for the above using a phenomenological model for the low energy excitations following Ref. [10]. An energy-symmetric fermionic density of states $D(E, B)$ of the form $D(E, 0) = \Gamma E^{-1}$ (Γ is some dimensionless constant) gives rise to $C_m/T \propto T^{-1}$ in zero field. In presence of a field, the DOS in the low-energy region below $\alpha\mu_B B$ (where α is some dimensionless constant) is written as $D(E, B) = \Gamma|E|^\gamma/(\alpha\mu_B B)^{\gamma+1}$. This models a

suppression of DOS at low energies. Such a DOS will lead to the observed scaling of C_m/T as shown in the inset of Fig. 5 (for details, see Ref. [23]).

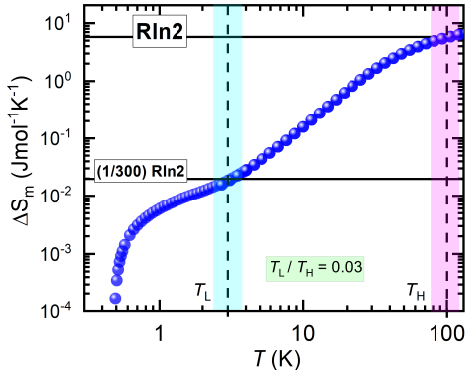


FIG. 6. Magnetic entropy change, ΔS_m as a function of temperature at zero field for $\text{H}_{5.9}\text{Li}_{0.1}\text{Ru}_2\text{O}_6$ (blue circles). The entropy corresponding to a $J_{\text{eff}} = \frac{1}{2}$ magnetic system ($R\ln 2$) is shown as a reference (the upper black horizontal line). Plateaus are seen at $T_L \sim 3$ K (vertical dotted line with light blue shade; from Z_2 -flux excitations putatively) and T_H (from itinerant Majorana excitations putatively) ~ 100 K (vertical dotted line with pink shade). The ratio of T_L/T_H is 0.03 consistent with isotropic Kitaev model.

From C_m , we compute the magnetic entropy change ΔS_m for the system at zero field using $\Delta S_m(T) = \int_{T_{\text{lowest}}}^T \frac{C_m}{T'} dT'$ where T_{lowest} is the lowest temperature measured in our experiments (500 mK). [27] Figure 6 shows ΔS_m vs. T . By about 100 K, a magnetic entropy value of $R\ln 2$ is recovered which is consistent with that for a $J_{\text{eff}} = 1/2$ system. Further, we see a two-step entropy release for HLRO. For a Kitaev spin liquid, the two step entropy release corresponds to the freeing up of two types of quasi-particles – Z_2 flux excitations at low- T (T_L) and itinerant Majorana fermions at a higher- T (T_H). In the idealized case, the entropy is released in two equal halves of $R\ln 2/2$ [28] and the ratio $\frac{T_L}{T_H} \sim 0.03$ [28–30]. We find that in HLRO the ratio $\frac{T_L}{T_H} \sim 0.03$ is consistent with the expected value, but the ratio for ΔS_m at the plateaus (1/300) does not match the expected value. We note that even for the field-induced KQSL in α - RuCl_3 above 80 kOe, a similar two-step entropy release has been observed and proposed as an evidence of Z_2 flux and itinerant Majorana fermions, but there are deviations from expected values. The ratio of $\frac{T_L}{T_H}$ in α - RuCl_3 is 0.22 and the appearance of $R\ln 2/2$ recovery at the lower-temperature plateau due to flux excitations is also unclear [29]. A small amount of vacancy and quasi-vacancy in HLRO might be affecting the first plateau in the entropy release due to bound-flux sector excitations as we have seen low temperature variation of $C_m/T \propto T^{-1}$ at zero field deviates from pure

Kitaev limit ($C_m/T \propto T$)[3]. Alternately, additional couplings such as Heisenberg and off-diagonal exchange terms has been shown as a possibility for the unequal entropy release [31–33]. Given the scalings observed in HLRO, the unequal entropy release may be ascribed to vacancy effects primarily.

Conclusion— We propose HLRO to be a Ru^{3+} -containing Kitaev QSL which shows no sign of long range ordering down to 500 mK and hence does not require a magnetic field to reveal Kitaev physics. We observed a scaling behaviour of the magnetic specific heat as $C_m/T \propto (T/B)^\gamma$ which is consistent with defect/vacancy-induced effects predicted for a KQSL due to weak localization of Majorana fermions. An apparent divergence of C_m/T with T^{-1} at low- T is also consistent with this picture. A two-step entropy release is inferred from heat capacity data and $T_L/T_H \sim 0.03$, a key signature of KQSL. The deviation from $R\ln 2/2$ (expected for a pristine KQSL) of the entropy release at the first step is suggested to arise from defects/vacancies as well. Whereas the presence of defects/vacancies is inevitable in a real material, here they serve as a probe of the pristine state. This then opens up a new direction for future work where the effect of vacancy concentration on the power law exponent can be investigated. This also provides motivation to carry out thermal Hall effect and inelastic neutron scattering measurements for further validating our conclusions.

I. ACKNOWLEDGMENT

We thank MOE STARS scheme for financial support. SP acknowledges funding support from SERB-DST, India via Grants No. MTR/2022/000386. We thank Eric Andrade, Ciarán Hickey, Edwin Kermarrec and Mohammad Monish for discussions. μSR experiments were performed at Paul Scherrer Institute (PSI), Switzerland with beam-time allocation ID: 20221240 on GPS, $S\mu\text{S}$ facility. Thanks to GPS, $S\mu\text{S}$ facility at PSI for beam-time allocation. We also thank MPI-CPFS, Dresden, Germany for financial support and access to measurement facilities. Thanks to IITB-central facilities for various measurements.

* sanjayphysics95@gmail.com

† mahajan@phy.iitb.ac.in

- [1] A. Kitaev, *Annals of Physics* **321**, 2 (2006), january Special Issue.
- [2] H. Takagi, T. Takayama, G. Jackeli, G. Khaliullin, and S. E. Nagler, *Nature Reviews Physics* **1**, 264 (2019).
- [3] W.-H. Kao, J. Knolle, G. B. Halász, R. Moessner, and N. B. Perkins, *Phys. Rev. X* **11**, 011034 (2021).

- [4] C. Hickey and S. Trebst, *Nature Communications* **10**, 530 (2019).
- [5] W.-H. Kao and N. B. Perkins, *Annals of Physics* **435**, 168506 (2021), special issue on Philip W. Anderson.
- [6] S.-H. Baek, S.-H. Do, K.-Y. Choi, Y. S. Kwon, A. U. B. Wolter, S. Nishimoto, J. van den Brink, and B. Büchner, *Phys. Rev. Lett.* **119**, 037201 (2017).
- [7] A. Banerjee, J. Yan, J. Knolle, C. A. Bridges, M. B. Stone, M. D. Lumsden, D. G. Mandrus, D. A. Tennant, R. Moessner, and S. E. Nagler, *Science* **356**, 1055 (2017), <https://www.science.org/doi/pdf/10.1126/science.aah6015>.
- [8] M. Majumder, M. Schmidt, H. Rosner, A. A. Tsirlin, H. Yasuoka, and M. Baenitz, *Phys. Rev. B* **91**, 180401 (2015).
- [9] S. C. Williams, R. D. Johnson, F. Freund, S. Choi, A. Jesche, I. Kimchi, S. Manni, A. Bombardi, P. Manuel, P. Gegenwart, and R. Coldea, *Phys. Rev. B* **93**, 195158 (2016).
- [10] K. Kitagawa, T. Takayama, Y. Matsumoto, A. Kato, R. Takano, Y. Kishimoto, S. Bette, R. Dinnebier, G. Jackeli, and H. Takagi, *Nature* **554**, 341 (2018).
- [11] B. J. Kim, H. Jin, S. J. Moon, J.-Y. Kim, B.-G. Park, C. S. Leem, J. Yu, T. W. Noh, C. Kim, S.-J. Oh, J.-H. Park, V. Durairaj, G. Cao, and E. Rotenberg, *Phys. Rev. Lett.* **101**, 076402 (2008).
- [12] S. Trebst and C. Hickey, *Physics Reports* **950**, 1 (2022), *kitaev materials*.
- [13] B. Zwartsenberg, R. P. Day, E. Razzoli, M. Michiardi, N. Xu, M. Shi, J. D. Denlinger, G. Cao, S. Calder, K. Ueda, J. Bertinshaw, H. Takagi, B. J. Kim, I. S. Elfimov, and A. Damascelli, *Nature Physics* **16**, 290 (2020).
- [14] A. Razpopov, D. A. S. Kaib, S. Backes, L. Balents, S. D. Wilson, F. Ferrari, K. Riedl, and R. Valentí, *npj Quantum Materials* **8**, 36 (2023).
- [15] S. Pei, L.-L. Huang, G. Li, X. Chen, B. Xi, X. Wang, Y. Shi, D. Yu, C. Liu, L. Wang, F. Ye, M. Huang, and J.-W. Mei, *Phys. Rev. B* **101**, 201101 (2020).
- [16] P. Bhattacharyya, N. A. Bogdanov, S. Nishimoto, S. D. Wilson, and L. Hozoi, *npj Quantum Materials* **8**, 52 (2023).
- [17] R. Kumar, T. Dey, P. M. Ette, K. Ramesha, A. Chakraborty, I. Dasgupta, J. C. Orain, C. Baines, S. Tóth, A. Shahee, S. Kundu, M. Prinz-Zwick, A. A. Gippius, N. Büttgen, P. Gegenwart, and A. V. Mahajan, *Phys. Rev. B* **99**, 054417 (2019).
- [18] S. A. J. Kimber, C. D. Ling, D. J. P. Morris, A. Chemseddine, P. F. Henry, and D. N. Argyriou, *J. Mater. Chem.* **20**, 8021 (2010).
- [19] T. Takayama, M. Blankenhorn, J. Bertinshaw, D. Haskel, N. A. Bogdanov, K. Kitagawa, A. N. Yaresko, A. Krajewska, S. Bette, G. McNally, A. S. Gibbs, Y. Matsumoto, D. P. Sari, I. Watanabe, G. Fabbri, W. Bi, T. I. Larkin, K. S. Rabinovich, A. V. Boris, H. Ishii, H. Yamaoka, T. Irifune, R. Bewley, C. J. Ridley, C. L. Bull, R. Dinnebier, B. Keimer, and H. Takagi, *Phys. Rev. Res.* **4**, 043079 (2022).
- [20] G. Khaliullin, *Phys. Rev. Lett.* **111**, 197201 (2013).
- [21] P. S. Anisimov, F. Aust, G. Khaliullin, and M. Daghofer, *Phys. Rev. Lett.* **122**, 177201 (2019).
- [22] J. c. v. Chaloupka and G. Khaliullin, *Phys. Rev. B* **100**, 224413 (2019).
- [23] For details see Supplemental Material at URL , which includes Refs. 3, 10, 17–19, 24, 25, 31–41.
- [24] D. J. Morgan, *Surface and Interface Analysis* **47**, 1072 (2015).
- [25] A. Chakraborty, V. Kumar, S. Bachhar, N. Büttgen, K. Yokoyama, P. K. Biswas, V. Siruguri, S. Pujari, I. Dasgupta, and A. V. Mahajan, *Phys. Rev. B* **104**, 115106 (2021).
- [26] Y.-X. Yang, L.-L. Huang, Z.-H. Zhu, C.-S. Chen, Q. Wu, Z.-F. Ding, C. Tan, P. K. Biswas, A. D. Hillier, Y.-G. Shi, D.-P. Yu, C. Liu, L. Wang, F. Ye, J.-W. Mei, and L. Shu [10.48550/ARXIV.2201.12978](https://arxiv.org/abs/2201.12978) (2022).
- [27] The magnitude of entropy change from low- T to about 100 K ($\sim R \ln 2$) does not change much if one extrapolates the magnetic heat capacity to zero at 0 K.
- [28] J. Nasu, M. Udagawa, and Y. Motome, *Phys. Rev. B* **92**, 115122 (2015).
- [29] S.-H. Do, S.-Y. Park, J. Yoshitake, J. Nasu, Y. Motome, Y. Kwon, D. T. Adroja, D. J. Voneshen, K. Kim, T.-H. Jang, J.-H. Park, K.-Y. Choi, and S. Ji, *Nature Physics* **13**, 1079 (2017).
- [30] Y. Motome and J. Nasu, *Journal of the Physical Society of Japan* **89**, 012002 (2020), <https://doi.org/10.7566/JPSJ.89.012002>.
- [31] Y. Yamaji, T. Suzuki, T. Yamada, S.-i. Suga, N. Kawashima, and M. Imada, *Phys. Rev. B* **93**, 174425 (2016).
- [32] A. Catuneanu, Y. Yamaji, G. Wachtel, Y. B. Kim, and H.-Y. Kee, *npj Quantum Materials* **3**, 23 (2018).
- [33] H. Li, D.-W. Qu, H.-K. Zhang, Y.-Z. Jia, S.-S. Gong, Y. Qi, and W. Li, *Phys. Rev. Res.* **2**, 043015 (2020).
- [34] S. Kundu, A. Shahee, A. Chakraborty, K. M. Ranjith, B. Koo, J. Sichelschmidt, M. T. F. Telling, P. K. Biswas, M. Baenitz, I. Dasgupta, S. Pujari, and A. V. Mahajan, *Phys. Rev. Lett.* **125**, 267202 (2020).
- [35] Y.-X. Yang, L.-L. Huang, Z.-H. Zhu, C.-S. Chen, Q. Wu, Z.-F. Ding, C. Tan, P. K. Biswas, A. D. Hillier, Y.-G. Shi, D.-P. Yu, C. Liu, L. Wang, F. Ye, J.-W. Mei, and L. Shu, Muon spin relaxation study of spin dynamics in quantum spin liquid candidate $\text{H}_3\text{LiIr}_2\text{O}_6$ (2022), [arXiv:2201.12978](https://arxiv.org/abs/2201.12978) [*cond-mat.str-el*].
- [36] C. Kittel and P. McEuen, *Introduction to solid state physics*, 8th ed. (John Wiley and Sons, Inc, 2005).
- [37] S. Kundu, A. Hossain, P. K. S., R. Das, M. Baenitz, P. J. Baker, J.-C. Orain, D. C. Joshi, R. Mathieu, P. Mahadevan, S. Pujari, S. Bhattacharjee, A. V. Mahajan, and D. D. Sarma, *Phys. Rev. Lett.* **125**, 117206 (2020).
- [38] Y. Miura, Y. Yasui, M. Sato, N. Igawa, and K. Kakurai, *Journal of the Physical Society of Japan* **76**, 033705 (2007), <https://doi.org/10.1143/JPSJ.76.033705>.
- [39] F. Bahrami, W. Lafargue-Dit-Hauret, O. I. Lebedev, R. Movshovich, H.-Y. Yang, D. Broido, X. Rocquefelte, and F. Tafti, *Phys. Rev. Lett.* **123**, 237203 (2019).
- [40] S. Bette, T. Takayama, K. Kitagawa, R. Takano, H. Takagi, and R. E. Dinnebier, *Dalton Trans.* **46**, 15216 (2017).
- [41] C. Lee, S. Lee, Y. Choi, C. Wang, H. Luetkens, T. Shiroka, Z. Jang, Y.-G. Yoon, and K.-Y. Choi, *Phys. Rev. B* **107**, 014424 (2023).

Supplementary Material for $(\text{H,Li})_6\text{Ru}_2\text{O}_6$: a zero-field Ru^{3+} -based Kitaev Quantum Spin Liquid

Sanjay Bachhar,^{1,*} M. Baenitz,² Hubertus Luetkens,³ Sumiran Pujari,¹ and A.V. Mahajan^{1,†}

¹Department of Physics, Indian Institute of Technology Bombay, Powai, Mumbai 400076, India

²Max Planck Institute for Chemical Physics of Solids, 01187 Dresden, Germany

³Laboratory for Muon Spin Spectroscopy, Paul Scherrer Institute, CH-5232 Villigen PSI, Switzerland
(Dated: May 13, 2024)

Polycrystalline $(\text{H,Li})_6\text{Ru}_2\text{O}_6$ are prepared through solid-state reaction followed by Hydrothermal method. X-ray diffraction evidences a single phase pure compound. The Ru-valency was determined by X-ray photoelectron spectroscopy (XPS). A systematic NMR spectral intensity calculation suggested the Li-content in the compound and H-content was estimated through charge balance. Then, we have measured magnetization, heat capacity and local probe (Nuclear Magnetic Resonance (NMR) and Muon Spin Relaxation (μSR)) to understand underlying physics of $(\text{H,Li})_6\text{Ru}_2\text{O}_6$. Herein, we report supplementary information of $(\text{H,Li})_6\text{Ru}_2\text{O}_6$: a zero-field Ru^{3+} -based Kitaev Quantum Spin Liquid.

I. SAMPLE PREPARATION

The preparation of $(\text{H,Li})_6\text{Ru}_2\text{O}_6$ samples, involves a two steps process, which was carried out at IIT Bombay facility. Li_2RuO_3 , precursor is prepared using the standard solid-state reaction method. Then, H-intercalation was carried out in Li_2RuO_3 using a hydrothermal method (similar method was used in preparation of $\text{H}_3\text{LiIr}_2\text{O}_6$, a KQSL [1]) that applies both pressure and temperature to the compound. This process do replacement of Li with H, forming a new compound. Depending on intercalation time, Li-quantity will vary (for details see VII) in resultant compound. The compound with 96 hours intercalation time, was carried out, the reduction of Li in the final sample was confirmed through a flame test of the by-product (which contained the extracted Li from Li_2RuO_3), and the structure was analyzed using X-ray diffraction. The valency of Ruthenium was determined using XPS, which showed that it was in the Ru^{3+} state. This led to the discovery of a reproducible 2D layered compound, $(\text{H,Li})_6\text{Ru}_2\text{O}_6$, which could serve as an alternative to $\alpha\text{-RuCl}_3$. To determine the amount of Li in $(\text{H,Li})_6\text{Ru}_2\text{O}_6$, we used the ^7Li -NMR Spectral intensity method, as described in section VII. Our investigation has shown that the relationship between intercalation time and Li content for Ir and Ru-based compounds is different. For the compound with 96 hours intercalation time, we found

that the Li content was approximately 2.5% relative to Li_2RuO_3 , leading to the chemical formula $\text{H}_{5.9}\text{Li}_{0.1}\text{Ru}_2\text{O}_6$ (HLRO) under charge balance.

II. X-RAY DIFFRACTION AND RIETVELD REFINEMENT

To check the phase purity of HLRO, we have measured the powder x-ray diffraction (XRD) of polycrystalline sample at IIT Bombay central facilities. The XRD data were collected at room temperature with $\text{Cu-K}\alpha$ radiation ($\lambda=1.54182 \text{ \AA}$) over the angular range $10^\circ \leq 2\theta \leq 90^\circ$ with a 0.013° step size.

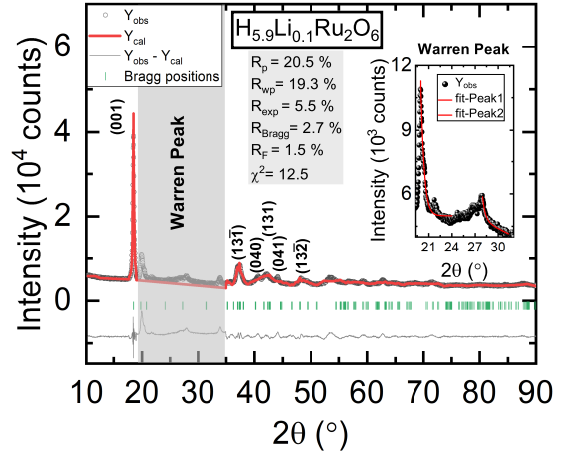


FIG. 1. The single phase Rietveld refinement of XRD pattern of $\text{H}_{5.9}\text{Li}_{0.1}\text{Ru}_2\text{O}_6$. The open black circles are the observed data, the red line is theoretically calculated one, the grey line is the difference between the observed and the calculated data and the green vertical marks are Bragg positions with corresponding Miller indices. Inset shows the Warren peak.

Figure 1 shows the single phase Rietveld refinement of HLRO. After the refinement, we found that the prepared HLRO crystallizes in the monoclinic C2/m space group with lattice parameter $a = 5.07 \text{ \AA}$, $b = 8.97 \text{ \AA}$, $c = 5.01 \text{ \AA}$, $\alpha = \gamma = 90^\circ$ and $\beta = 106.8^\circ$. The goodness of the Rietveld refinement is defined by the following parameters; $\chi^2 = 12.5$, $R_p = 20.5\%$, $R_{wp} = 19.3\%$, $R_{exp} = 5.5\%$. Table I summarizes the unit cell parameters and quality factors for the Rietveld refinement of HLRO.

* sanjayphysics95@gmail.com

† mahajan@phy.iitb.ac.in

A Warren peak is observed in the range 19° to 35° , shown in inset of Figure 1 with a fit [2] as given below,

$$I_w(2\theta) = Ae^{-g(2\theta)^2} + B/(C + (2\theta)^2), \quad (1)$$

where A, B and C are constants, g is the exponent of the Gaussian term and it measures the percentage of the stacking faults known as the g -factor:

$$g = \delta^2/d^2, \delta^2 = \langle d^2 \rangle - \langle d \rangle^2 \quad (2)$$

where d is the interlayer spacing. A good fit with exponent, $g = 0.06(6)$ in the inset of Figure 1 corresponds to at least 6% volume fraction of stacking disorder. After excluding the Warren peak, Rietveld refinement is performed with faultless model (stacking faults are ignored) to extract different quality factors, atomic coordinates, site occupancies, and the isotropic Debye-Waller factors ($B_{iso} = 8\pi^2 U_{iso}$) of HLRO, which are tabulated in Table I and Table II respectively.

TABLE I. Unit cell parameters and quality factors are reported for the Rietveld refinement of $H_{5.9}Li_{0.1}Ru_2O_6$ at room temperature.

Unit Cell Parameters for C2/m		Quality Factors	
a(Å)	5.07(3)		
b(Å)	8.97(4)	R_{Bragg} (%)	2.7
c(Å)	5.01(2)	R_F (%)	1.5
$\alpha = \gamma$ (°)	90	R_{exp} (%)	5.5
β (°)	106.8(8)	R_p (%)	20.5
Z	2	R_{wp} (%)	19.3
V (Å ³)	218.3(4)	χ^2	12.5

TABLE II. Atomic coordinates, Normalized site occupancies, and the isotropic Debye-Waller factors ($B_{iso} = 8\pi^2 U_{iso}$) are reported for the Rietveld refinement of $H_{5.9}Li_{0.1}Ru_2O_6$.

Atom	Wyckoff position	Site	x	y	z	Norm. Site Occ.	B_{iso} (Å ²)
Ru(1)	4g	2	0	0.333	0	2	0.1
Li(1)	2a	2/m	0	0	0	0.1	0.1
O(1)	4i	m	0.417	0	0.22	2	1.7
O(2)	8j	1	0.404	0.323	0.229	4	1.7
H(1)	4h	2	0	0.161	1/2	2	0.1
H(2)	2d	2/m	1/2	0	1/2	3	0.1
H(3)	2a	2/m	0	0	0	0.9	0.1

III. X-RAY PHOTOELECTRON SPECTROSCOPY (XPS)

X-ray photoelectron spectroscopy (XPS) is a surface-sensitive technique that is based on the photoelectric effect. It is used to determine the elemental composition and chemical state of a material, as well as the electronic structure and density of the electronic states in the material. XPS is a powerful technique because it not only shows which elements are present, but also how they are bonded to other elements. The chemical states are inferred from the binding energy and number of ejected electrons. X-ray photoelectron spectroscopy (XPS) is

also one of the most popular method to investigate valency of elements present in a compound. In order to know valency of Ru in HLRO, XPS spectra were measured at Central Surface Analytical Facility (ESCA lab) at IIT Bombay. The C1s reference position was taken as 284.7 eV for all the materials. After modeling and fitting the spectra in ESCape software, the data was exported to an Excel sheet and plotted in Origin software. RuO_2 (precursor of HLRO) which is a good example of Ru^{4+} compound, was measured to use as a reference to investigate XPS spectra of HLRO.

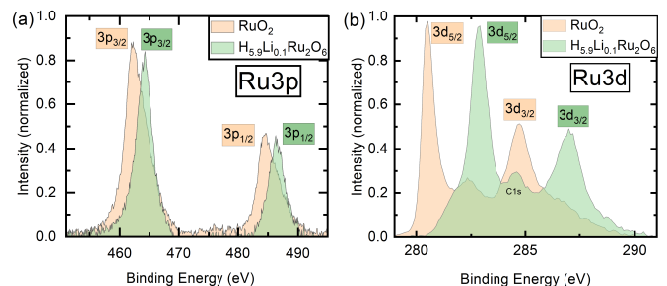


FIG. 2. (a) $Ru3p$ XPS spectra of $H_{5.9}Li_{0.1}Ru_2O_6$ with reference to RuO_2 . (b) $Ru3d$ XPS spectra of $H_{5.9}Li_{0.1}Ru_2O_6$ with reference to RuO_2 .

TABLE III. Binding energies for $H_{5.9}Li_{0.1}Ru_2O_6$, RuO_2 and $RuCl_3$.

Material	Peak	Binding Energy (eV)	Oxidation State	Comments
HLRO	$3d_{5/2}$	282.9	3+	Present Study.
	$3d_{3/2}$	287		
	$3p_{3/2}$	464.2		
	$3p_{1/2}$	486.3		
$RuCl_3$	$3d_{5/2}$	282.8	3+	Taken from reference [3].
	$3d_{3/2}$	287		
	$3p_{3/2}$	464.1		
RuO_2	$3d_{5/2}$	280.5	4+	Present Study and also its consistent with reference [3].
	$3d_{3/2}$	284.7		
	$3p_{3/2}$	462.2		
	$3p_{1/2}$	484.7		

Figure 2(a) shows $Ru3p$ XPS spectra of HLRO with reference to RuO_2 . There is clear right shift in $3p_{3/2}$ and $3p_{1/2}$. Figure 2(b) shows $Ru3d$ XPS spectra of HLRO with reference to RuO_2 . There is also clear right shift in $3d_{5/2}$ and $3d_{3/2}$. Shift in both $Ru3p$ and $Ru3d$ spectra indicates valency of Ru in HLRO is not in 4+ state. We analysed XPS spectra by using ESCape software to extract Binding energies of different peaks and it is shown in table III. Binding energies of $Ru3d_{5/2}$, $Ru3d_{3/2}$ and $Ru3p_{3/2}$ in HLRO are consistent with $RuCl_3$ where Ru is in 3+ state as reported in literature [3]. That indicates Ru in HLRO is in 3+ state.

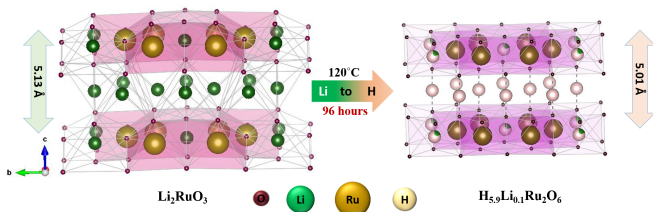


FIG. 3. The crystal structure of Li_2RuO_3 (left) that can be transformed into $\text{H}_{5.9}\text{Li}_{0.1}\text{Ru}_2\text{O}_6$ (right) by 96 hours H-intercalation (Hydrothermal Method).

IV. CRYSTAL STRUCTURE

Figure 3 depicts the crystal structures of $\text{H}_{5.9}\text{Li}_{0.1}\text{Ru}_2\text{O}_6$ (space group $C2/m$) and its precursor, Li_2RuO_3 (space group $P21/m$). The precursor, Li_2RuO_3 , undergoes strong dimerization at temperatures below ~ 540 K, resulting in the formation of molecular orbitals (MOs)[4]. In contrast, intercalation has been found to suppress Ru-Ru dimerization in $\text{Ag}_3\text{LiRu}_2\text{O}_6$ [5–7]. The H-intercalation process for 96 hours at 120°C led to the replacement of Li atoms by H atoms from both the inter-layer positions and the in-plane positions (partially). The contraction of the c -parameter of the lattice (from 5.13 Å to 5.01 Å) due to the lighter H atoms replacing the inter-layered Li atoms is illustrated in Figure 3. The structural analysis reveals a perfect honeycomb network with a $\text{Ru} - \text{Ru}$ bond distance of ~ 2.96 Å and a $d - p - d$ bond angle of $\sim 95^\circ$. The presence of Ru^{3+} (as indicated by XPS analysis) at the vertices of this perfect honeycomb network makes it a Kitaev honeycomb system, serving as an alternative to $\alpha\text{-RuCl}_3$.

V. MAGNETIZATION

The dc magnetization $M(T)$ as a function of temperature (T , range 2-300 K) was measured on a cold pressed pellet of HLRO in zero field cooled (ZFC) at 10 kOe field, also in zero field cooled (ZFC)-field cooled (FC) mode at 50 Oe and $M(H)$ vs H (magnetic field) at 20 K using a Quantum Design Magnetic Property Measurement System (MPMS). The main features of our observations from the measurement are described below.

Figure 4 shows M vs H at 20 K in the field range (-70 kOe to 70 kOe). We observe that it is a perfect linear isotherm ($M(H) = \chi H$, where χ is susceptibility) passing through origin $(0,0)$ of M vs H at 20 K plot. That indicates there is no ferromagnetic impurity present in system. Then, we calculated χ by using $\chi = M/H$. The bulk magnetic susceptibility, χ shows a cross over around 40 K which has also been observed in other techniques such as specific heat, NMR and μSR , as can be found in the respective sections later. No sharp anomaly down to 2 K has been seen in χ vs T (300 K to 2 K) plot in main

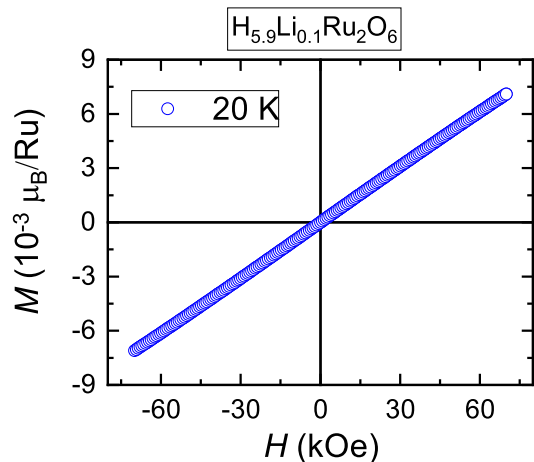


FIG. 4. M vs H at 20 K in the field range (-70 kOe to 70 kOe).

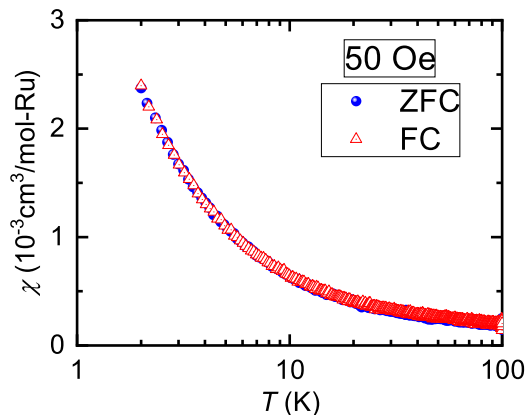


FIG. 5. No bifurcation in the the semi-log plot of $\chi(T)$ vs. T between zero field cooled (ZFC) (blue sphere) and field cooled (FC) (red triangle) mode at an applied field $H = 50$ Oe in the temperature range 100 K to 2 K.

paper. This feature rules out the presence of any kind of either long-range ordering (LRO) or frozen magnetism within the system. Curie-Weiss fitting ($\chi = \chi_0 + \frac{C}{T - \theta_{CW}}$) in the temperature range 100-300 K (black solid line on red square symbol of $1/(\chi - \chi_0)$ vs. T plot) reveals $\chi_0 = 3.69 \times 10^{-5} \text{ cm}^3/\text{mol-Ru}$, Curie-Weiss temperature ~ -44 K and effective moment $\sim 0.43 \mu_B$ which is 4 times smaller than the effective moment corresponding to a pure $J_{eff} = 1/2$ system. No bifurcation in plot of $\chi(T)$ vs. T between ZFC-FC mode at an applied field $H = 50$ Oe (Figure 5) in the temperature range 100 K to 2 K rules out possibility of static/glassy moment present in the system.

VI. HEAT CAPACITY

To get more information about low-energy excitations, we measured the heat capacity of the sample at constant pressure $C_p(T)$ in the temperature range (500 mK-300 K) at 0 kOe and in the temperature range (400 mK-40 K) at 10-60 kOe for HLRO and non-magnetic analog $\text{Li}_3\text{LiSn}_2\text{O}_6$ in the temperature range 1.8-300 K.

In general total specific heat, C_p of the system can be expressed as:

$$C_p(T, H) = C_{lattice}(T) + C_{Sch}(T, H) + C_m(T, H) \quad (3)$$

The lattice specific heat is denoted as $C_{lattice}$, while C_{Sch} represents the Schottky contribution caused by independent paramagnetic spins present in the system. The remaining magnetic contribution to the specific heat is referred to as C_m . Our main objective is to determine the "intrinsic" magnetic contribution C_m , which is independent of $C_{lattice}$ and C_{Sch} . To obtain the intrinsic C_m , we must first calculate $C_{lattice}$ and C_{Sch} , and then deduct them from the total specific heat C_p . There are a few ways to calculate $C_{lattice}$. A prominent way is to measure heat capacity of a suitable non-magnetic analog and another way is Debye-Einstein fitting[8].

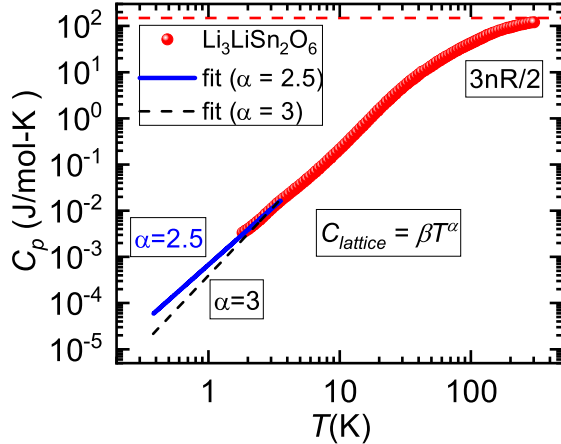


FIG. 6. Specific heat, C_p per Sn as a function of temperature for $\text{Li}_3\text{LiSn}_2\text{O}_6$ (red sphere). blue solid line and black dot line are fitted curve with $\alpha = 2.5$ and $\alpha = 3$ respectively.

We have a suitable non-magnetic analog $\text{Li}_3\text{LiSn}_2\text{O}_6$ (see Figure 6) as a heat capacity reference of HLRO. We have measured the heat capacity of $\text{Li}_3\text{LiSn}_2\text{O}_6$ from 300 K to 1.8 K. At high temperature, value of C_p should be $3nR$ (n is number of atoms per formula unit, R is gas constant) according to Dulong-Petit law[9]. We plotted C_p per Sn in Figure 6, so we expected $3nR/2$ at 300 K. We observe C_p of $\text{Li}_3\text{LiSn}_2\text{O}_6$ at 300 K matching with $3nR/2$ reference line (pink dash line). At low- T , lattice

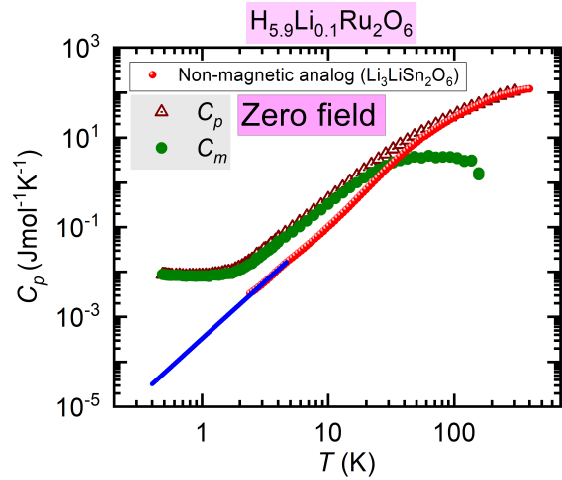


FIG. 7. Specific heat, C_p per Ru as a function of temperature for $\text{H}_{5.9}\text{Li}_{0.1}\text{Ru}_2\text{O}_6$ (wine triangle). The non-magnetic analog is shown by red sphere followed by blue line (extrapolated part). Magnetic heat capacity, C_m is also shown in the same plot by olive circle.

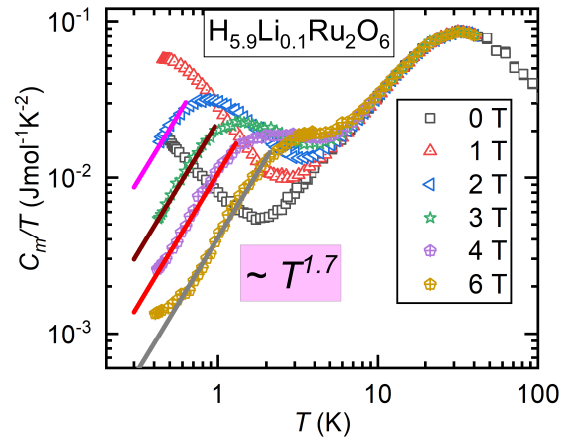


FIG. 8. C_m/T versus T for various fields: 0-6 Tesla where C_m is the magnetic heat capacity.

heat capacity should follow power law ($C_{lattice} \sim \beta T^3$) theoretically (black dotted line is shown in Figure 6). We fitted data to $C_{lattice} \sim \beta T^\alpha$ in the temperature range 1.8-3.6 K and it yields $\beta = 0.0007$ and $\alpha = 2.5$. Then, we extrapolated the data from 1.8 K to 400 mK for C_m calculation. Note that at 500 mK, C_p of $\text{Li}_3\text{LiSn}_2\text{O}_6$ value $\sim 10^{-4}$ which is 1/100 th of measured C_p of HLRO (that is $\sim 10^{-2}$). So, small error ($\Delta \alpha = 0.5$) in $C_{lattice}$ at low- T does not affect C_m much.

Figure 7 shows specific heat, C_p as a function of temperature for $\text{H}_{5.9}\text{Li}_{0.1}\text{Ru}_2\text{O}_6$ (wine triangle), non-magnetic analog $\text{Li}_3\text{LiSn}_2\text{O}_6$ (red sphere). Magnetic heat capacity, C_m (olive circle) for $\text{H}_{5.9}\text{Li}_{0.1}\text{Ru}_2\text{O}_6$ is shown at the same plot in log-log scaling to clearly

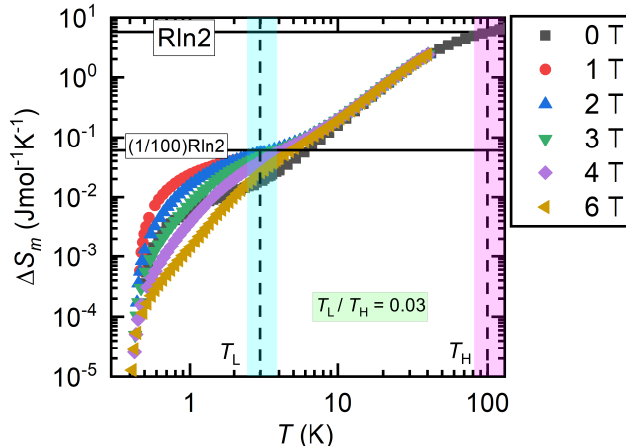


FIG. 9. Magnetic entropy change, ΔS_m as a function of temperature at various fields: 0-6 T for $\text{H}_{5.9}\text{Li}_{0.1}\text{Ru}_2\text{O}_6$. The entropy corresponding to a $J_{eff} = \frac{1}{2}$ magnetic system ($Rln2$) is shown as a reference (the upper black horizontal line).

show low-T features. The specific heat of the magnetic and non-magnetic analogs is expected to match at high temperatures (typically 100-300 K) with scaling of the Debye-temperature, which depends on the molar mass of the compound. In zero field, C_m is the difference between as-measured C_p and $C_{lattice}$ (that is C_p of nonmagnetic analog) since $C_{sch} = 0$ at zero field. We calculated C_m and it is shown in the Figure 7 with as-measured C_p of $\text{H}_{5.9}\text{Li}_{0.1}\text{Ru}_2\text{O}_6$ and C_p of $\text{Li}_3\text{LiSn}_2\text{O}_6$. No anomaly down to 500 mK indicates absence of long range magnetic ordering. In $\text{H}_3\text{LiIr}_2\text{O}_6$, there is a power law increase of $C_p/T \propto T^{-1/2}$ and does not approach zero at $T = 0$, indicating presence of highly degenerate low-lying excitations around $E = 0$. The C_p and C_m at low- T are nearly the same because lattice contribution is negligible (below 1 K, it is $\sim 10^{-3}$ to 10^{-5} $\text{Jmol}^{-1}\text{K}^{-1}$). In $\text{H}_{5.9}\text{Li}_{0.1}\text{Ru}_2\text{O}_6$, C_m does not approach zero at $T \rightarrow 0$ like in $\text{H}_3\text{LiIr}_2\text{O}_6$. That indicates system is not gapped. In zero magnetic field, C_m/T diverges with T^{-1} below about 4 K could be due to vacancy (missing magnetic atom) and quasi-vacancy (spinless impurity on a magnetic site) induced low-energy density of states in the Kitaev Spin Liquid[10]. Hence, the ground state will have bound flux in zero magnetic field instead of flux-free sector for pure Kitaev ($C_m/T \propto T$). With the application of a magnetic field, ground state becomes flux-free for higher fields[10]. Figure 8 shows C_m/T as a function of temperature. C_m/T is field dependent and follows power law ($\sim T^{1.7}$) variation. These are indication of a gapless excitations from a novel ground state. After obtaining C_m , we proceeded to compute the magnetic entropy change ΔS_m (given by $\Delta S_m = \int C_m/T dT$) for the system at zero field. Figure 9 shows magnetic entropy, ΔS_m as a function of temperature at various fields: 0-6 Tesla for HLRO.

At 100 K, magnetic entropy value $Rln2$ is recovered. Since $Rln2$ is corresponds to $J_{eff} = 1/2$ spins entropy, we claim HLRO is a Ru^{3+} with $J_{eff} = 1/2$. There is a two step entropy release in HLRO like in $\alpha\text{-RuCl}_3$ except the first step of the release is not at $Rln2/2$. ΔS_m is field dependent and suppress with increasing field similar like C_m . We conjecture that the two step entropy release corresponds to the freeing up of two types of quasiparticles of the KQSL; Z_2 flux at low- T feature and itinerant Majorana Fermions at the high- T feature. However, the ratio of ΔS_m at the two plateau is about $1/100$ against the expected value of $1/2$, but the ratio of the two corresponding temperature, $T_L/T_H \sim 0.03$ is consistent with the expected value of 0.03 in the isotropic Kitaev model. So far only $\alpha\text{-RuCl}_3$, a field induced KQSL reveals two step entropy release features as an evidence of Z_2 flux and itinerant Majorana fermions. There are also distinct differences from expected values: (i) $(1/2)Rln2$ recovery at T_H instead of onset of T_L , (ii) ratio of $T_L/T_H \sim 0.22$ against the expected value of 0.03 in the isotropic Kitaev model. A small amount of vacancy and quasi-vacancy in HLRO might be affecting the first plateau in the entropy release due to bound-flux sector excitations as we have seen low temperature variation of $C_m/T \propto T^{-1}$ at zero field deviates from pure Kitaev limit ($C_m/T \propto T$)[10]. Alternately, additional couplings such as Heisenberg and off-diagonal exchange terms has been shown as a possibility for the unequal entropy release [11–13]. Given the scalings observed in HLRO, the unequal entropy release may be ascribed to vacancy effects primarily.

VII. NUCLEAR MAGNETIC RESONANCE

NMR is a useful local probe of low energy excitations in magnetic insulators. For a recent example of a NMR study on a Kitaev honeycomb system, see Reference[14]. In our system, the probe nucleus, ^7Li sits at the center of Ru-honeycomb in octahedral environment which leads to zero electric field gradient.

A. ^7Li NMR

The nucleus ^7Li is an ideal candidate for NMR investigations due to its $I = 3/2$ nuclear spin and 92.6% natural abundance. The gyromagnetic ratio of ^7Li is 16.54 MHz/Tesla. For our NMR study of the $\text{H}_{5.9}\text{Li}_{0.1}\text{Ru}_2\text{O}_6$ sample, we utilized a Cu-coil with a frequency range of 90-180 MHz, and the sample's mass was 376 mg. Two types of solid-state-NMR were used for measurement. One is persistent magnet NMR (Fourier Transform NMR) and another is NMR with fixed frequency and variable field (Field Sweep NMR). We exposed the sample to a homogeneous magnetic field of approximately 93.95 kOe (persistent magnet) and excited the target nucleus with a radio frequency (rf)

pulse equal to its Larmour frequency (ω_0). The spectra were obtained by Fourier transforming the spin-echo after a $\pi/2-\pi$ pulse sequence. We determined the spin-lattice relaxation time (T_1) using a saturation recovery pulse sequence with a $\pi/2$ pulse of 5 ms.

1. ${}^7\text{Li}$ NMR Spectra

Li-quantitative analysis We measured ${}^7\text{Li}$ NMR spectra at 300 K for various H-intercalated samples (intercalation time: 2, 6, 32, 96 hours) and precursor- Li_2RuO_3 ($\text{Li}_4\text{Ru}_2\text{O}_6$) (Figure 10).

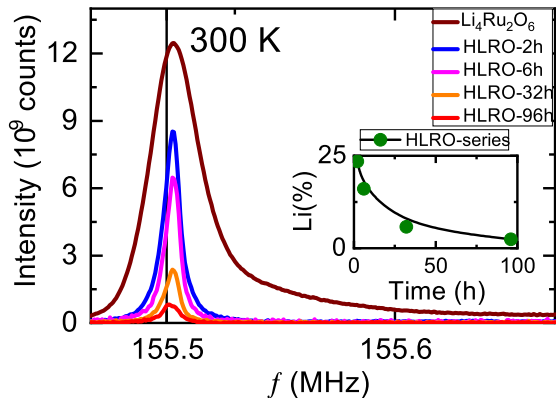


FIG. 10. Various ${}^7\text{Li}$ NMR Spectra for precursor- $\text{Li}_4\text{Ru}_2\text{O}_6$ and sets of HLRO named after intercalation time; HLRO-2h, HLRO-6h, HLRO-32h, HLRO-96h. Inset shows Li content variation as a function of intercalation time.

The solid black line is the reference position at 155.457 MHz. The brown color broad line corresponds to ${}^7\text{Li}$ NMR spectra of the precursor- $\text{Li}_4\text{Ru}_2\text{O}_6$. There is no shift in spectral line of $\text{Li}_4\text{Ru}_2\text{O}_6$. The possible reason is weak hyperfine coupling although system is magnetic. The y-axis is the absolute intensity scaled by molar mass. In order to compare different spectra, we have kept all technical NMR parameters same for all samples. The blue, pink, yellow, red lines are ${}^7\text{Li}$ NMR spectra for HLRO-2h, HLRO-6h, HLRO-32h, HLRO-96h respectively. There are also no shift in NMR spectra, same as precursor- $\text{Li}_4\text{Ru}_2\text{O}_6$. But a narrowing of the NMR line compared to $\text{Li}_4\text{Ru}_2\text{O}_6$ is observed. That indicates amount of Li present in HLRO-series is less than that in $\text{Li}_4\text{Ru}_2\text{O}_6$. The absolute intensity gradually decreases with increasing intercalation time of sample. We calculated the Li per formula unit of HLRO-series by the equation;

$$\frac{I_{abs}(H_x\text{Li}_y\text{Ru}_2\text{O}_6)}{I_{abs}(\text{Li}_4\text{Ru}_2\text{O}_6)} = \frac{y}{4} \quad (4)$$

where $I_{abs}(H_x\text{Li}_y\text{Ru}_2\text{O}_6)$ is the absolute ${}^7\text{Li}$ NMR

spectral intensity of $H_x\text{Li}_y\text{Ru}_2\text{O}_6$ (HLRO-series) and $I_{abs}(\text{Li}_4\text{Ru}_2\text{O}_6)$ is the absolute ${}^7\text{Li}$ NMR spectral intensity of $\text{Li}_4\text{Ru}_2\text{O}_6$. We calculated absolute ${}^7\text{Li}$ NMR spectral intensity for all samples: HLRO-2h, HLRO-6h, HLRO-32h, HLRO-96h. The ratio of intensity in percentage are shown in inset of Figure 10. In HLRO, the percentage of Li is decreasing with increasing intercalation time. Finally, Li per formula unit is calculated by equation 4 and it is 1, 0.6, 0.2, 0.1 for HLRO-2h, HLRO-6h, HLRO-32h, HLRO-96h respectively. We have XPS evidence of Ru valency of HLRO-96h which is +3. HLRO-96h with Li = 0.1 (per formula unit) and Ru^{3+} , leads to H= 5.9 (per formula unit) under charge balance. That leads to the formula $\text{H}_{5.9}\text{Li}_{0.1}\text{Ru}_2\text{O}_6$ for HLRO-96h. The compound HLRO-96h or $\text{H}_{5.9}\text{Li}_{0.1}\text{Ru}_2\text{O}_6$ is called as HLRO throughout main paper as well as supplementary materials.

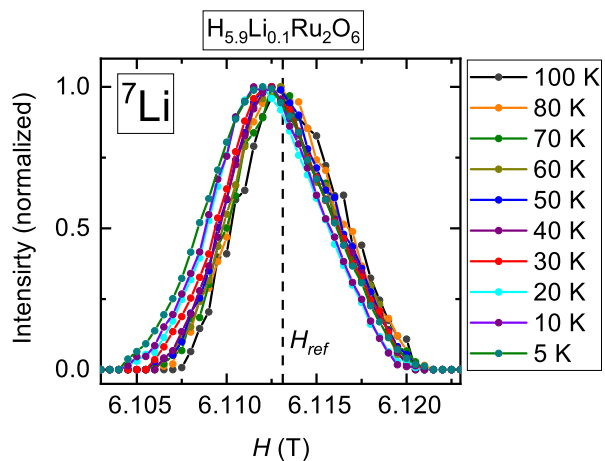


FIG. 11. ${}^7\text{Li}$ NMR field sweep spectra at 100.29 MHz in the temperature range 5-100 K. the black dotted line is the reference position, H_{ref} .

Figure 11 shows ${}^7\text{Li}$ NMR field sweep spectra of HLRO at 100.29 MHz in the temperature range 5-100 K. The black dotted line is the reference position, H_{ref} . We observe there is almost no shift down to 50 K, then change to non-zero-shift followed by a leveling-off below 20 K. We observe there is almost no change in line broadening down to 10 K and slight broadening at 5 K spectra.

NMR Shift, 7K and FWHM We have fitted the spectra to Gaussian function to obtain peak position and FWHM value. We have shown one field sweep spectrum (5 K) fitting in Figure 12. We calculated NMR shift, ${}^7K \sim 200$ ppm and FWHM ~ 80 Oe at 5 K. Figure 13 (left y-axis) shows variation of NMR Shift, 7K with temperature, T . There is a clear change in ${}^7K \sim 40$ K and then levels off below 20 K. This is indeed consistent with bulk magnetic susceptibility as there was also broad anomaly ~ 40 K. The temperature independent non-zero (~ 200 ppm) 7K below 20 K might be a signature

of QSL. Figure 13 (right y-axis) shows FWHM (full width half maxima) variation with temperature. We observe a constant FWHM down to 10 K and then slight increase at 5 K. That indicates internal field distribution is independent of temperature like KQSL, $\text{H}_3\text{LiIr}_2\text{O}_6$ [14].

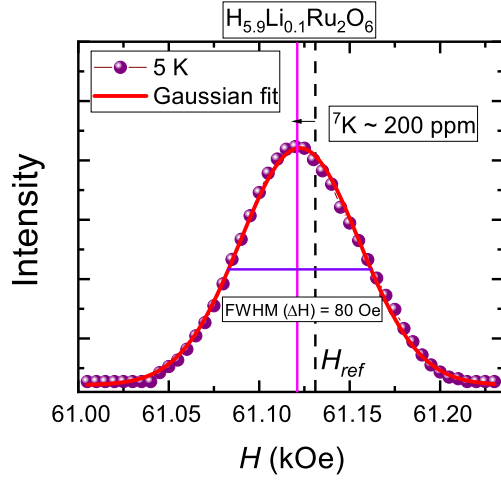


FIG. 12. ^7Li NMR field sweep spectra (frequency = 100.29 MHz) at 5 K. The black dotted line is the reference position, H_{ref} .

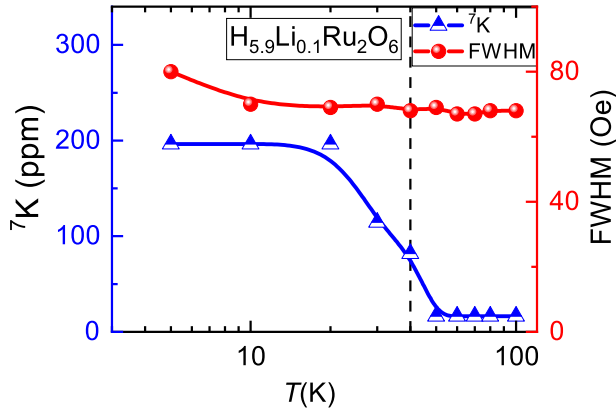


FIG. 13. The left y-axis shows variation of NMR Shift, ^7K with temperature, T . The right y-axis shows FWHM (full width half maxima) with T .

2. ^7Li Spin-lattice relaxation rate, $1/T_1$

The Figure 14 shows the variation of $1/T_1$ as a function of temperature for $\text{H}_{5.9}\text{Li}_{0.1}\text{Ru}_2\text{O}_6$ at different applied magnetic fields (40 kOe, 61.11 kOe and 80 kOe) in the temperature range 2-150 K. The anomaly ~ 40

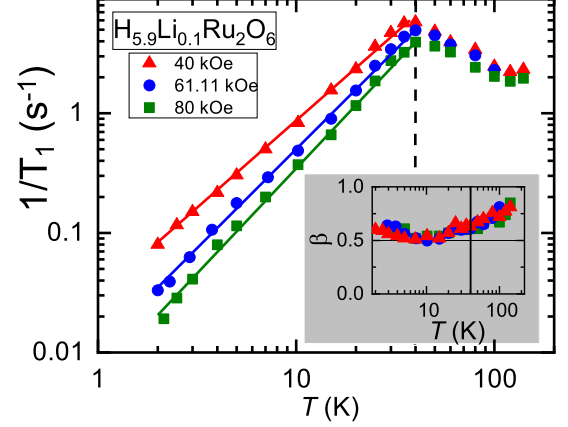


FIG. 14. The Variation of $1/T_1$ as a function of temperature for $\text{H}_{5.9}\text{Li}_{0.1}\text{Ru}_2\text{O}_6$ at different applied magnetic fields: 40 kOe (red triangle), 61.11 kOe (blue circle), 80 kOe (green square). (Inset) Stretch exponent, β vs Temperature, T .

K has been also observed in other measurements like magnetization and heat capacity. Below 40 K, $1/T_1$ exhibits a power law variation with temperature. While the anomaly at ~ 40 K is not likely due to long range ordering (LRO) or glassy magnetism (no evidence in $\chi(T)$ or $C_m(T)$), the power law suggests gapless excitations. The spin lattice relaxation rate, $1/T_1$ suppressed below 40 K with increasing applied field. A similar effect was seen in $\text{H}_3\text{LiIr}_2\text{O}_6$ and was attributed to field dependent density of states (DOS).

B. ^1H NMR

The nucleus ^1H is an ideal candidate for NMR investigations due to its $I = 1/2$ nuclear spin and 99.98% natural abundance. The gyromagnetic ratio of ^1H is 42.575 MHz/Tesla. In $\text{H}_{5.9}\text{Li}_{0.1}\text{Ru}_2\text{O}_6$, ^1H occupied inter layer as well in-plane position. The spectra were obtained by field sweep method at MPI-CPFS, dresden. We determined the spin-lattice relaxation time (T_1) using a saturation recovery pulse sequence with a $\pi/2$ pulse of 3 ms.

1. ^1H NMR Spectra

Figure 15 shows ^1H NMR field sweep spectra in the temperature range 5-100 K. We observe that there is no shift and also independent of temperature. The line width, FWHM is also constant. That indicates internal field distribution is same. We have seen such scenario in KQSL, $\text{H}_3\text{LiIr}_2\text{O}_6$.

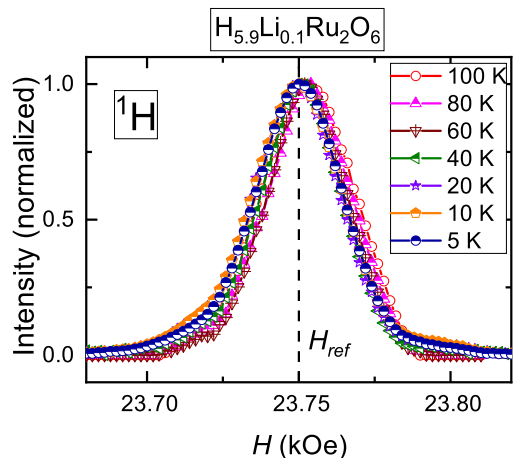


FIG. 15. ^1H NMR field sweep spectra in the temperature range 5-100 K for $\text{H}_{5.9}\text{Li}_{0.1}\text{Ru}_2\text{O}_6$. The black dotted line is the reference position, H_{ref} .

2. ^1H Spin-lattice relaxation rate, $1/T_1$

Figure 16 shows variation of spin-lattice relaxation rate, $1/T_1$ as a function of temperature for $\text{H}_{5.9}\text{Li}_{0.1}\text{Ru}_2\text{O}_6$ at 15.54 kOe and 23.75 kOe and also for probe. We observe $1/T_1$ has a peak around 150 K and then a minimum ~ 40 K. Below 40 K, it has another broad anomaly around 10 K followed by a power law variation. The variation of $1/T_1$ for 15.54 kOe (blue square) and 23.75 kOe (red triangle) are similar but quantitative values are different. We observe $1/T_1$ value for empty probe is close to $\text{H}_{5.9}\text{Li}_{0.1}\text{Ru}_2\text{O}_6$ down to 40 K. It looks $1/T_1$ for probe also varies with temperature. Commenting on $1/T_1$ data above 40 K is risky because separation of probe contribution from measured sample data looks tricky. However, T_1 at 10 K for probe and HLRO are factor of 5 difference with constant stretch exponent, $\beta \sim 0.75$. Below 10 K, power law variation of spin lattice relaxation rate ($\sim T^{0.8-0.9}$) indicates gapless excitation.

VIII. MUON SPIN RELAXATION (μSR)

Zero field μSR at 1.56 K The Oscillations in ZF- μSR are key signature for magnetically ordered system below transition temperature [15]. Magnetic spins get order and muon spins precess about static internal field. In presence of static spins, 1/3 of the local magnetic field components pointing parallel to the initial muon spin (and are therefore unchanged by the magnetic field) which gives rise to 1/3-tail in muon asymmetry and 2/3 of the magnetic field components in a perpendicular direction which gives rise to oscillations in asymmetry. If spins are dynamic and internal local field fluctuate continuously, exponential decay in asymmetry

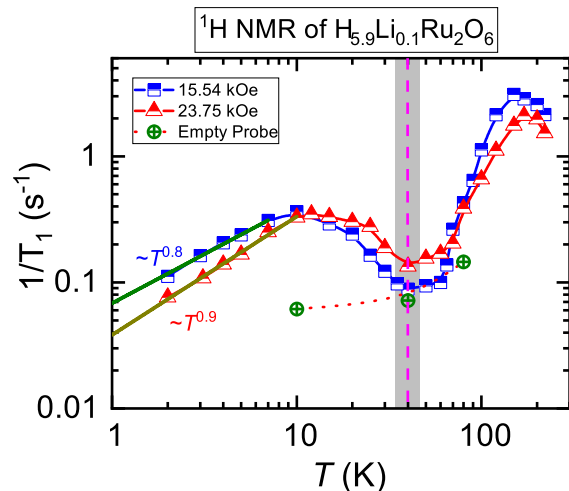


FIG. 16. The Variation of ^1H $1/T_1$ as a function of temperature for $\text{H}_{5.9}\text{Li}_{0.1}\text{Ru}_2\text{O}_6$ at 15.54 kOe (blue square) and 23.75 kOe (red triangle). The variation of $1/T_1$ for probe is shown by green circle.

is expected without any 1/3-tail. We performed zero field μSR at 1.56 K. We do not observe any oscillation. That indicates there is no long range ordering. We also do not observe any 1/3-tails. That indicates absence of static moments. Fitting the data to single exponential ($A(t) = A(0)\exp(-\lambda t)$) yields $\lambda = 0.7$ MHz, does not fit well. Then, we tried with stretch exponential ($A(t) = A(0)\exp(-(\lambda t)^\beta)$) (fitting parameter $\lambda = 0.68$ MHz and $\beta = 0.6$) which is also does not fit either, not fitting short time asymmetry decay properly. Finally, fitting to the data with double exponential function ($A(t) = A(0)[A_1\exp(-\lambda_1 t) + A_2\exp(-\lambda_2 t) + (1 - (A_1 + A_2))]$) looks the best fit which yields $A_1 = 0.256$ with $\lambda_1 = 19.8$ MHz and $A_2 = 0.70$ with $\lambda_2 = 0.48$ MHz.

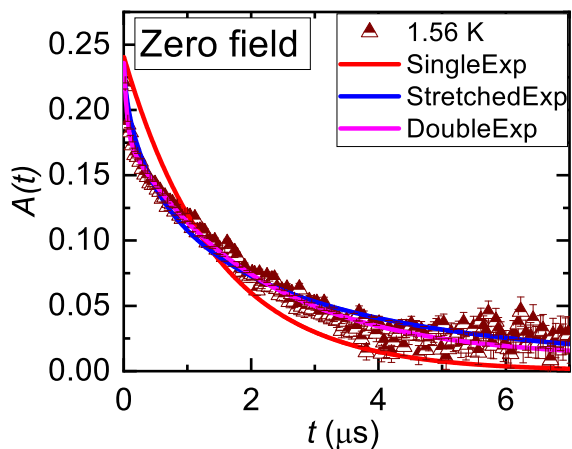


FIG. 17. Muon asymmetry as a function of decay time for zero field (ZF) at 1.56 K.

100 Oe-LF μ SR (1.56-300 K) Zero field μ SR measurements include contribution from nuclear and magnetic/electronic part. We applied a longitudinal field (LF) of 100 Oe which should remove the depolarization due to nuclear moments. Data were taken as a function of temperature between 1.56 K and 300 K in the longitudinal field of 100 Oe (Figure 18). The relaxation/depolarization thus observed should be only due to the electronic moments. We observe data between 1.56 K and 20 K overlaps indication of same relaxation rate λ . Above 20 K, data gradually changes its slope and exponential decay nature noticed even at 300 K.

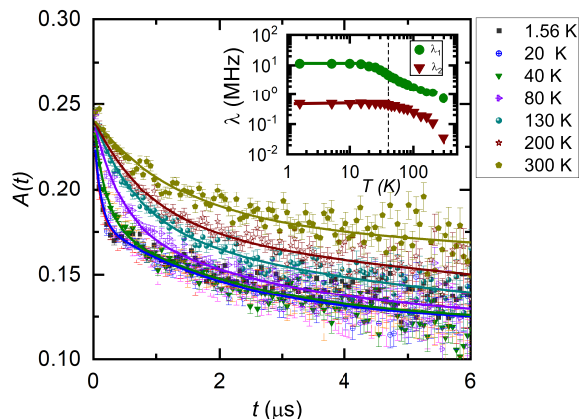


FIG. 18. Muon asymmetry as a function of decay for 100 Oe longitudinal field in the temperature range: 1.56 K-300 K. (Inset) Muon relaxation rate λ as a function of temperature. Two components of relaxation, λ_1 (olive circle) and λ_2 (wine circle) with $A_1 : A_2 = 1:1$ are observed.

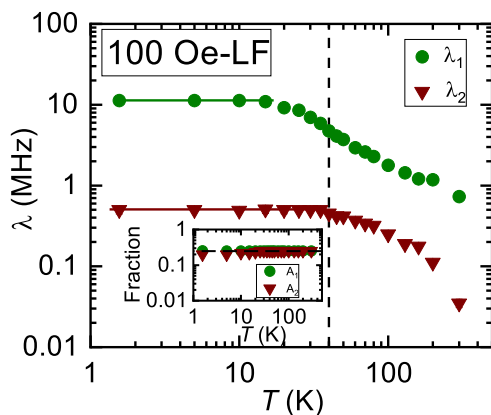


FIG. 19. Muon asymmetry as a function of decay for 100 Oe longitudinal field in the temperature range: 1.56 K-300 K. (Inset) Muon relaxation rate, λ as a function of temperature. Two components of relaxation, λ_1 (olive circle) and λ_2 (wine circle) with $A_1 : A_2 = 1:1$ are observed.

We found the muon relaxation could be best fit with a double exponential in addition to a constant as in $\text{H}_3\text{LiIr}_2\text{O}_6$. Figure 19 shows variation of λ_1 and λ_2 as function of temperature. Two components of relaxation, λ_1 and λ_2 with equal relative weights ($A_1 : A_2 = 1:1$) are observed. Muon spin relaxation rate, λ gradually increasing with lowering the temperature and there is a change in dynamics around ~ 40 K followed by a leveling-off below 20 K. Features at 40 K have been also observed in other bulk and NMR local probes which is a possible indication of a QSL cross over point. The flattening/saturation of λ at low- T indicates spin remains dynamic down to low- T . The weights (A_1 and A_2) are temperature-independent (see Figure 19 (Inset)). That indicates two muon stopping sites are present. Muon (μ^+) usually stops ~ 1 Å away from Oxygen (O). Possibly there is two O^{2-} sites crystallographically in a given unit cell. These results are similar to those of $\text{H}_3\text{LiIr}_2\text{O}_6$ except that the flattening/saturation of λ sets in at 10 times the temperature in $\text{H}_3\text{LiIr}_2\text{O}_6$ [16].

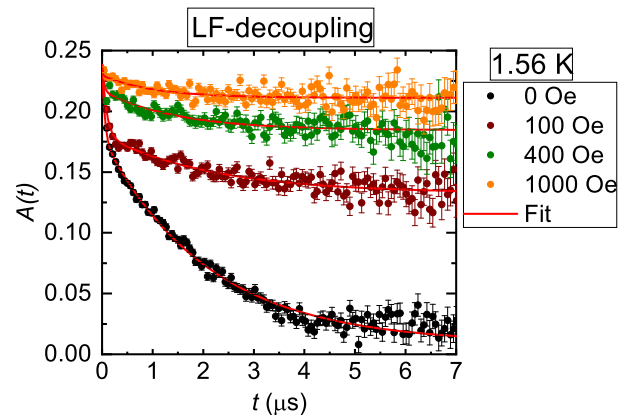


FIG. 20. Muon asymmetry as a function of decay time at 1.56 K for various longitudinal fields: 0 Oe, 100 Oe, 400 Oe, 1000 Oe.

LF-decoupling at 1.56 K Longitudinal field (LF) measurements are useful to differentiate between static and dynamic magnetism. If the magnetism is static, a longitudinal field with a strength 10 times greater than the field distribution would effectively decouple the muons. On the other hand, if the magnetism is dynamic, a longitudinal field 50 times stronger than the field distribution would be necessary. The nuclear field is ~ 2 -3 Oe and hence 50 Oe longitudinal field is enough to remove nuclear contribution. We applied 100-1000 Oe longitudinal field at 1.56 K to differentiate between static and dynamic spins (Figure 20). In HLRO, ZF/LF-muon asymmetry was well fitted with two exponential plus a constant rather than usual single exponential [17]. In our case, it probably arises from two muon stopping sites. There is no decoupling for the first component of

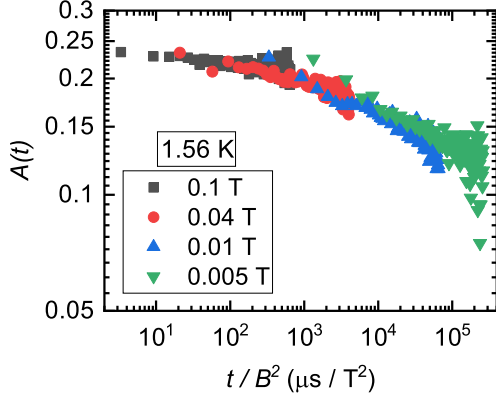


FIG. 21. Time-field scaling of LF- μ SR spectra at 1.56 K.

exponential decay (one of the muon stopping site) with application of 1000 Oe field. That indicates that the spins are dynamic. The second component (2nd muon stopping site) decoupling is observed. In systems with dilute spins, tail of asymmetry moves upward and parallel to each other to regain full polarization with an application of a large longitudinal field. In case of slow dynamics, there will be change in slope in tail of asymmetry as it moves upward to regain full polarization with an application of a longitudinal field. We conjecture that two muon stopping sites provides fast and slow component of λ from one magnetic environment of HLRO. Figure 21 shows time-field scaling of LF- μ SR spectra at 1.56 K. There is some connection between field dependent DOS (Density of States) and this scaling. We observed field dependent NMR- $1/T_1$ and C_m as an indication of field dependent DOS. We also found time-field scaling in the form $A(t) \sim t/H^\alpha$ with $\alpha = 2$. We suggest that this time-field scaling is connected to field dependent DOS as seen in $\text{H}_3\text{LiIr}_2\text{O}_6$ [16].

IX. MODEL OF DENSITY OF STATES (DOE)

Heat capacity can be written as

$$\frac{C}{T} = \frac{1}{T} \int ED(E) \frac{df(T, E)}{dT} dE \quad (5)$$

where $f(T, E)$ is Fermi distribution function and can be expressed as

$$f(T, E) = \frac{1}{\exp(E/k_B T) + 1} \quad (6)$$

For scaling, lets assume $E' = E/k_B T$. Hence, Equation 5 would be

$$\frac{C}{T} = k_B \int D(E' k_B T) \frac{E' \exp(E')}{(\exp(E') + 1)^2} dE' \quad (7)$$

For magnetic field, $B = 0$ if we model $D(E, 0) = \Gamma|E|^{-n}$ (where Γ is a constant with appropriate dimensions for $n = 0, 1, 2, \dots$)

then,

$$\frac{C}{T} \propto |T|^{-n} \quad (8)$$

For $n = 0.5$, we get $\frac{C}{T} \propto |T|^{-0.5}$ and $D(E, 0) \propto |E|^{-0.5}$ – the case for $\text{H}_3\text{LiIr}_2\text{O}_6$ [14].

For $n = 1$, $\frac{C}{T} \propto |T|^{-1}$ which is the case for our compound HLRO ($B = 0$) and hence $D(E, 0) = \Gamma|E|^{-1}$ with Γ being dimensionless. Following along the lines of Ref. [14], for $B \neq 0$, we model $D(E, B)$ as $\Gamma \frac{|E|^x}{(\alpha \mu_B B)^y}$ where x and y are variable but has the constraint of $y - x = 1$ from dimension analysis.

For $y = 2$ and $x = 1$ from equation 7, we obtain,

$$B \frac{C}{T} \propto \left(\frac{|T|}{B} \right) \quad (9)$$

For $y = 3$ and $x = 2$ from equation 7, we obtain,

$$B \frac{C}{T} \propto \left(\frac{|T|}{B} \right)^2 \quad (10)$$

For $y = 2.7$ and $x = 1.7$ from equation 7, we obtain,

$$B \frac{C}{T} \propto \left(\frac{|T|}{B} \right)^{1.7} \quad (11)$$

Equation 11 is the closest to the observation for our compound HLRO for $B \neq 0$.

X. SCALING IN M , C_m AND $1/T_1$

At low- T , bulk susceptibility (magnetization measurement) behaves like conventional Curie-Weiss ($\chi_{bulk} \propto T^{-1}$) due to magnetic defects (of extrinsic) where intrinsic susceptibility (NMR Shift) is independent of temperature, a reminiscent of QSL. However, $\chi_{bulk} \propto T^{-n}$ ($0 < n < 1$) is due to magnetic defects of intrinsic origin like vacancy, quasi-vacancy, bond-randomness and so on. $\chi_{bulk} \propto T^{-0.5}$ was found in $\text{H}_3\text{LiIr}_2\text{O}_6$ [14] and different values of $n=0.68$ is reported [18] (sample dependency). Figure 22 shows magnetic susceptibility, χ as function of temperature for various fields in the range 1-70 kOe. The green dot line indicates low- T upturn of χ_{bulk} ($\sim T^{-0.9}$). With an application of magnetic field, it suppressed and become

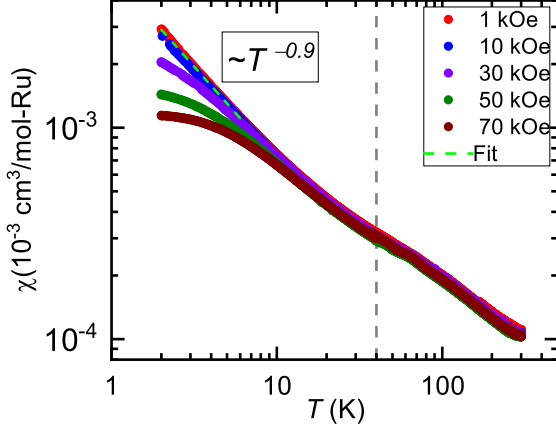


FIG. 22. Magnetic susceptibility, χ as function of temperature for various fields in the range 1-70 kOe. The green dot line indicates low- T upturn of χ_{bulk} ($\sim T^{-0.9}$).

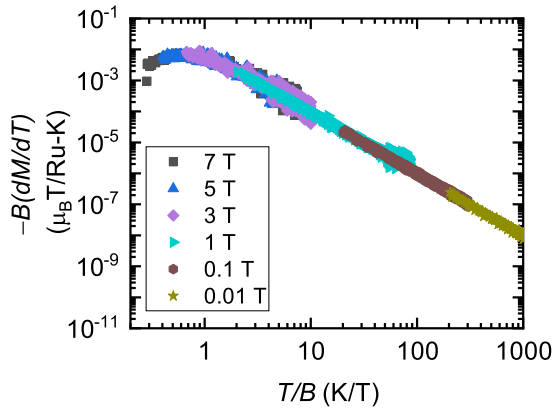


FIG. 23. A scaling of $B(dM/dT)$ with T/B

almost T -independent at 70 kOe. The behavior is qualitatively similar like $\text{H}_3\text{LiIr}_2\text{O}_6$ [14] but exponent is different in our case. We speculate presence of magnetic defects in the form of vacancy and quasi-vacancy. The effects of vancancy and quasi-vacancy has been seen in zero field C_m ($\propto T^{-1}$) as well (theoretical simulation can be found in literature [10]). We found a scaling of $B(dM/dT)$ with T/B (Figure 23). Magnetic heat capacity is also field dependent and shows a scaling of $B(C_m/T)$ with T/B . This arises from field dependent density-of-states as seen in $\text{H}_3\text{LiIr}_2\text{O}_6$ [14]. We found that the phenomenological model $D(E, B) = \frac{|E|^{1.7}}{(\alpha\mu_B B)^{2.7}}$ explains well our experimental results of C_m .

The susceptibility from defect regions is expected to have a power law increase with decreasing temperature. While this shows up as an upturn with decreasing

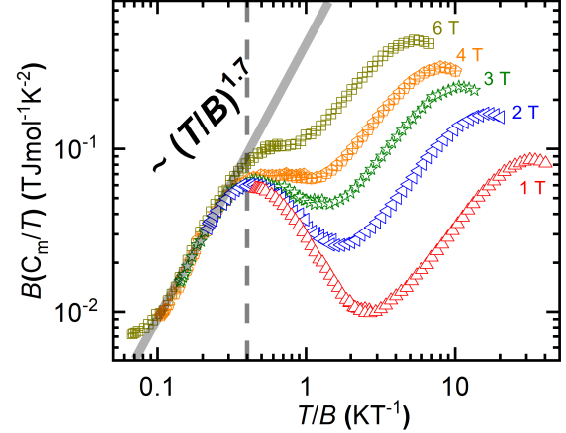


FIG. 24. A scaling of $B(C_m/T)$ with T/B

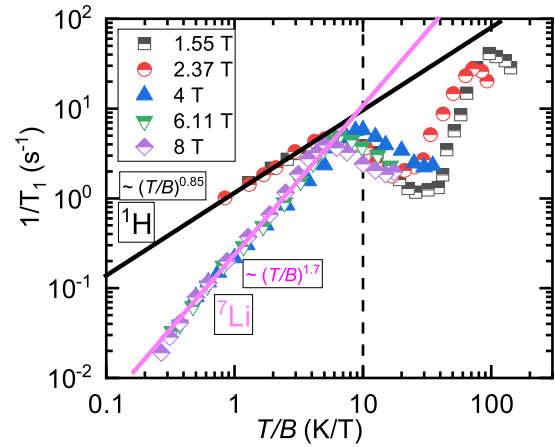


FIG. 25. The temperature-field scaling of ${}^7\text{Li}$ -Spin-lattice relaxation rate, $1/T_1$ with exponent ~ 1.7 and ${}^1\text{H}$ -Spinlattice relaxation rate, $1/T_1$ with exponent ~ 0.85 for $\text{H}_{5.9}\text{Li}_{0.1}\text{Ru}_2\text{O}_6$. The data for ${}^1\text{H}$ are multiplied by 13.24 to overlap with those for ${}^7\text{Li}$.

temperature in the bulk susceptibility, the NMR line shape should have a contribution (from defects) which has a power law increase in the shift with decreasing temperature. At low temperature, the defect contribution should then be well separated from the main resonance line. Consequently, in our T_1 measurements, where the transmitter frequency is centered on the main line, we are insensitive to the defect contribution (which is out of our spectral width). We observed field-dependent $1/T_1$ and a temperature-field scaling of ${}^7\text{Li}$ -Spin-lattice relaxation rate, $1/T_1$ with exponent ~ 1.7 and ${}^1\text{H}$ -Spinlattice relaxation rate, $1/T_1$ with exponent ~ 0.85 for $\text{H}_{5.9}\text{Li}_{0.1}\text{Ru}_2\text{O}_6$. This also arises from field-dependent density of states but not same as $D(E, B) =$

$\frac{|E|^{1.7}}{(\alpha\mu_B B)^{2.7}}$ (valid for C_m). Intrinsic magnetic defects (vacancy and quasi-vacancy) does effect the ground states. The picture in HLRO is that ground state has

bound Z_2 flux in low fields in presence of vacancies. The zero-flux KQSL is obtained upon the application field. The power law scaling is consistent with gapless excitations which we ascribed to the zero-flux KQSL and weak localization of Majorana fermions.

-
- [1] S. Bette, T. Takayama, K. Kitagawa, R. Takano, H. Takagi, and R. E. Dinnebier, *Dalton Trans.* **46**, 15216 (2017).
- [2] F. Bahrami, W. Lafargue-Dit-Hauret, O. I. Lebedev, R. Movshovich, H.-Y. Yang, D. Broido, X. Rocquefelte, and F. Tafti, *Phys. Rev. Lett.* **123**, 237203 (2019).
- [3] D. J. Morgan, *Surface and Interface Analysis* **47**, 1072 (2015).
- [4] Y. Miura, Y. Yasui, M. Sato, N. Igawa, and K. Kakurai, *Journal of the Physical Society of Japan* **76**, 033705 (2007), <https://doi.org/10.1143/JPSJ.76.033705>.
- [5] S. A. J. Kimber, C. D. Ling, D. J. P. Morris, A. Chemseddine, P. F. Henry, and D. N. Argyriou, *J. Mater. Chem.* **20**, 8021 (2010).
- [6] T. Takayama, M. Blankenhorn, J. Bertinshaw, D. Haskel, N. A. Bogdanov, K. Kitagawa, A. N. Yaresko, A. Krajewska, S. Bette, G. McNally, A. S. Gibbs, Y. Matsumoto, D. P. Sari, I. Watanabe, G. Fabbris, W. Bi, T. I. Larkin, K. S. Rabinovich, A. V. Boris, H. Ishii, H. Yamaoka, T. Irifune, R. Bewley, C. J. Ridley, C. L. Bull, R. Dinnebier, B. Keimer, and H. Takagi, *Phys. Rev. Res.* **4**, 043079 (2022).
- [7] R. Kumar, T. Dey, P. M. Ette, K. Ramesha, A. Chakraborty, I. Dasgupta, J. C. Orain, C. Baines, S. Tóth, A. Shahee, S. Kundu, M. Prinz-Zwick, A. A. Gippius, N. Büttgen, P. Gegenwart, and A. V. Mahajan, *Phys. Rev. B* **99**, 054417 (2019).
- [8] S. Kundu, A. Hossain, P. K. S., R. Das, M. Baenitz, P. J. Baker, J.-C. Orain, D. C. Joshi, R. Mathieu, P. Mahadevan, S. Pujari, S. Bhattacharjee, A. V. Mahajan, and D. D. Sarma, *Phys. Rev. Lett.* **125**, 117206 (2020).
- [9] C. Kittel and P. McEuen, *Introduction to solid state physics*, 8th ed. (John Wiley and Sons, Inc, 2005).
- [10] W.-H. Kao, J. Knolle, G. B. Halász, R. Moessner, and N. B. Perkins, *Phys. Rev. X* **11**, 011034 (2021).
- [11] Y. Yamaji, T. Suzuki, T. Yamada, S.-i. Suga, N. Kawashima, and M. Imada, *Phys. Rev. B* **93**, 174425 (2016).
- [12] A. Catuneanu, Y. Yamaji, G. Wachtel, Y. B. Kim, and H.-Y. Kee, *npj Quantum Materials* **3**, 23 (2018).
- [13] H. Li, D.-W. Qu, H.-K. Zhang, Y.-Z. Jia, S.-S. Gong, Y. Qi, and W. Li, *Phys. Rev. Res.* **2**, 043015 (2020).
- [14] K. Kitagawa, T. Takayama, Y. Matsumoto, A. Kato, R. Takano, Y. Kishimoto, S. Bette, R. Dinnebier, G. Jackeli, and H. Takagi, *Nature* **554**, 341 (2018).
- [15] A. Chakraborty, V. Kumar, S. Bachhar, N. Büttgen, K. Yokoyama, P. K. Biswas, V. Siruguri, S. Pujari, I. Dasgupta, and A. V. Mahajan, *Phys. Rev. B* **104**, 115106 (2021).
- [16] Y.-X. Yang, L.-L. Huang, Z.-H. Zhu, C.-S. Chen, Q. Wu, Z.-F. Ding, C. Tan, P. K. Biswas, A. D. Hillier, Y.-G. Shi, D.-P. Yu, C. Liu, L. Wang, F. Ye, J.-W. Mei, and L. Shu [10.48550/ARXIV.2201.12978](https://arxiv.org/abs/10.48550/ARXIV.2201.12978) (2022).
- [17] S. Kundu, A. Shahee, A. Chakraborty, K. M. Ranjith, B. Koo, J. Sichelschmidt, M. T. F. Telling, P. K. Biswas, M. Baenitz, I. Dasgupta, S. Pujari, and A. V. Mahajan, *Phys. Rev. Lett.* **125**, 267202 (2020).
- [18] C. Lee, S. Lee, Y. Choi, C. Wang, H. Luetkens, T. Shiroka, Z. Jang, Y.-G. Yoon, and K.-Y. Choi, *Phys. Rev. B* **107**, 014424 (2023).